




Article

Performance of Statistical and Intelligent Methods in Estimating Rock Compressive Strength

Xuesong Zhang ^{1,*}, Farag M. A. Altalbawy ^{2,3} , Tahani A. S. Gasmalla ⁴, Ali Hussein Demin Al-Khafaji ⁵, Amin Iraj ⁶, Rahmad B. Y. Syah ⁷  and Moncef L. Nehdi ^{8,*} 

¹ College of Pipeline and Civil Engineering, China University of Petroleum (East China), Qingdao 266580, China

² Department of Chemistry, University College of Duba, University of Tabuk, Tabuk 71491, Saudi Arabia

³ National Institute of Laser Enhanced Sciences (NILES), University of Cairo, Giza 12613, Egypt

⁴ Department of Education, University College of Duba, University of Tabuk, Tabuk 71491, Saudi Arabia

⁵ Department of Laboratories, Techniques, Al-Mustaqbal University College, Babylon, Hillah 51001, Iraq

⁶ Engineering Faculty of Khoy, Urmia University of Technology, Urmia 5716693188, Iran

⁷ PUIN-Engineering Faculty, Universitas Medan Area, Medan 20223, Indonesia

⁸ Department of Civil Engineering, McMaster University, Hamilton, ON L8S 4M6, Canada

* Correspondence: snowpiner@upc.edu.cn (X.Z.); nehdim@mcmaster.ca (M.L.N.); Tel.: +905-525-9140 (ext. 23824) (M.L.N.)

Abstract: This research was conducted to forecast the uniaxial compressive strength (UCS) of rocks via the random forest, artificial neural network, Gaussian process regression, support vector machine, K-nearest neighbor, adaptive neuro-fuzzy inference system, simple regression, and multiple linear regression approaches. For this purpose, geo-mechanical and petrographic characteristics of sedimentary rocks in southern Iran were measured. The effect of petrography on geo-mechanical characteristics was assessed. The carbonate and sandstone samples were classified as mudstone to grainstone and calc-litharenite, respectively. Due to the shallow depth of the studied mines and the low amount of quartz minerals in the samples, the rock bursting phenomenon does not occur in these mines. To develop UCS predictor models, porosity, point load index, water absorption, P-wave velocity, and density were considered as inputs. Using variance accounted for, mean absolute percentage error, root-mean-square-error, determination coefficient (R^2), and performance index (PI), the efficiency of the methods was evaluated. Analysis of model criteria using multiple linear regression allowed for the development of a user-friendly equation, which proved to have adequate accuracy. All intelligent methods (with $R^2 > 90\%$) had excellent accuracy for estimating UCS. The percentage difference of the average of all six intelligent methods with the measured value was equal to +0.28%. By comparing the methods, the accuracy of the support vector machine with radial basis function in predicting UCS was ($R^2 = 0.99$ and $PI = 1.92$) and outperformed all the other methods investigated.

Keywords: UCS; intelligent and statistical methods; prediction; sedimentary rocks



Citation: Zhang, X.; Altalbawy, F.M.A.; Gasmalla, T.A.S.; Al-Khafaji, A.H.D.; Iraj, A.; Syah, R.B.Y.; Nehdi, M.L. Performance of Statistical and Intelligent Methods in Estimating Rock Compressive Strength. *Sustainability* **2023**, *15*, 5642. <https://doi.org/10.3390/su15075642>

Academic Editors: Mahdi Hasanipanah, Danial Jahed Armaghani, Jian Zhou and Jianjun Ma

Received: 27 December 2022

Revised: 26 February 2023

Accepted: 15 March 2023

Published: 23 March 2023



Copyright: © 2023 by the authors. Licensee MDPI, Basel, Switzerland. This article is an open access article distributed under the terms and conditions of the Creative Commons Attribution (CC BY) license (<https://creativecommons.org/licenses/by/4.0/>).

1. Introduction

Stability of slopes, prediction of drilling rate, classification of rock masses, and modeling of foundations require knowledge of the uniaxial compressive strength (UCS) of the rocks for designing projects [1–3]. Indirect determination of the UCS in places where the preparation of standard samples is difficult requires lots of time and is expensive. Hence, various researchers have predicted the UCS of the limestones and sandstones using statistical and intelligent methods [4–7]. Aladejare et al. [8] collected empirical relationships and models between UCS and other rock characteristics from previous studies. Several models were developed to estimate the rock UCS using Gaussian process regression (GPR) [9–13], feedforward multilayer perceptron artificial neural network (FMP-ANN) [14–19], random forest algorithm (RFA) [20–23], adaptive neuro-fuzzy inference system (ANFIS) [24–28],

and multiple linear regression (MPLR) [3,4,7,8,25,29–31]. The results of Lawal et al.'s [9] study showed that the GPR method, with a correlation coefficient of almost 100%, is able to estimate the static and dynamic properties of sedimentary rocks. Moreover, a comparison of the RFA, MPLR, FMP-ANN methods in compressive strength estimation showed that FMP-ANN with the Levenberg–Marquardt algorithm has a higher accuracy than other methods [20]. The results of Matin et al.'s [22] study to select the effective variables using the random forest method showed that compression wave velocity is the most effective variable as an input for estimating compressive strength and the modulus of elasticity using predictive models. Hudaverdi [25] stated that the ANFIS method has a high efficiency in flyrock estimation with an average error of less than 8%. The results of the MPLR, ANFIS, and FMP-ANN methods in the UCS estimation showed that all three methods have a determination coefficient higher than 90%, while the ANFIS method has a better performance [26]. The comparison of the ANFIS, FMP-ANN and multiple regression methods by Yesiloglu-Gultekin and Gokceoglu [26] showed that the ANFIS method has higher accuracy for estimating compressive strength and the modulus of elasticity.

Mahmoodzadeh et al. [32] compared the K-nearest neighbor algorithm (KNN), Gaussian process regression based on squared exponential kernel (GPR-SEK), support vector machine with radial basis function (SVR-RBF), and decision tree (DT) methods to forecast rock quality designation in a tunnel project and stated that the GPR-SEK method is more accurate than other methods. Xu et al. [33] forecasted the UCS of rock using intelligent techniques. The SVM-RBF was used to predict UCS [34]. Rastegarnia et al. [19] used FMP-ANN and MPLR to predict the UCS of carbonates. They stated that FMP-ANN estimates the UCS more than the measured value. Trott et al. [35] used RFA to classify rock types. Barzegar et al. [36] predicted the UCS of travertine rocks using the SVM-RBF, FMP-ANN, and ANFIS methods and stated that the SVM-RBF showed higher accuracy than the other methods. Mohamad et al. [37] estimated the UCS of soft rocks using FMP-ANN and particle swarm optimization (PSO)-based ANN. Madhubabu et al. [6] used MPLR and FMP-ANN to estimate the UCS of the carbonate samples. Umrao et al. [24] used the ANFIS approach for estimating UCS based on density, porosity, and PWV. Moreover, using intelligent methods, Gül et al. [17] predicted the UCS of different rock types. Singh et al. [38] estimated the UCS of basalt samples via MPLR and ANFIS. Kaloop et al. [39] used GPR and multivariate adaptive regression splines (MARSs) to estimate rock UCS. They stated that the MARS showed higher accuracy than the GPR method. Some engineers and researchers are interested in simple empirical relationships using simple models such as simple and MPLR to estimate UCS. Therefore, simple empirical relationships are widely used to estimate rock UCS using statistical methods. Table 1 shows some of the relationships for estimating UCS by previous researchers.

This study was conducted to predict the UCS of sedimentary rocks based on porosity, point load index (PLI), density (D), water absorption by weight (WW), and P-wave velocity (PWV) using the FMP-ANN, GPR-SEK, KNN, RFA, ANFIS, SVM, SR, and MPLR methods. Moreover, the types of kernel functions were investigated using the SVM method and the most accurate type of kernel function was introduced to estimate the UCS.

Sampling points, from 12 mines in the Bushehr province, south of Iran, are located between 50 and 52 degrees longitudes and 28 and 30 degrees latitudes. The mines are mainly travertine, limestone, and sandstone of the Aghajari and the Mishan formations.

Table 1. Relationships for estimating UCS by previous researchers.

Equation	Reference	Lithology
$UCS = 12.29PLI^{1.233}$	Teymen and Mengüç [40]	Various Rocks
$UCS = -37.82 + (0.017PWV)$	Salehin [41]	Sedimentary Rocks
$UCS = 0.043PWV - 136.8$	Aldeeky and Al Hattamleh [42]	Basalt Rocks
$UCS = 17.6PLI + 13.5$	Aliyu et al. [30]	Sedimentary Rocks
$UCS = 14.3PLI$	Aladejare [8]	Sedimentary Rocks
$UCS = 9.95PWV^{(1.21)}$	Kahraman [43]	Sedimentary rocks
$UCS = 0.034PWV - 86.36$	Wen et al. [7]	Limestone
$UCS = -5.10\phi + 110.79$	Edet [3]	Sandstone
$UCS = 0.025PWV - 8.619$	Azimian [29]	Limestone
$UCS = 6.6PWV^{1.6}$	Uyanık et al. [44]	Sedimentary rocks
$UCS = 22.18PWV - 30.32$	Selcuk and Nar [31]	Various Rocks
$UCS = 0.041PWV - 15.40$	Abdi and Khanlari [4]	Sandstones
$UCS = 2.304(PWV)^{2.43}$	Kılıç and Teyman [45]	Various Rocks
$UCS = 10 - 5D^{16.7}$	Aladejare [8]	Sedimentary rocks

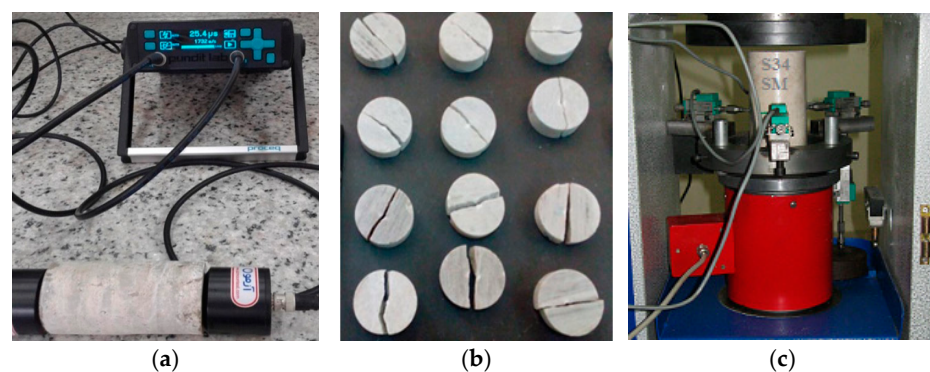
2. Methodology

2.1. Laboratory Tests

Specimens with a diameter of 54 mm and a height to diameter ratio of 2 were prepared [46]. A wear device was used to parallel surfaces of specimens. Table 2 shows the methods used to measure geo-mechanical properties. Figure 1 displays some of the samples in laboratory tests.

Table 2. Methods used for performing tests.

Test	Standards and References	Descriptions
UCS	ISRM [47]	A constant loading rate of 0.7 MPa per second was applied to the samples. The amount of deformation was recorded using the corresponding gauge in the UCS test. This test was done on irregular and cylindrical samples. Then the PLI was calculated.
Point load index (PLI)	ASTM D5731 [48]	With a $\frac{1}{2}$ MHz frequency
Compressional wave velocity test	ASTM D2845 [49]	The total porosity (ϕ) of specimens was measured using the method of saturation and immersion way. Density was computed from the ratio of mass to sample volume.
Porosity (ϕ), density(D) and water absorption by weight (WW)	ISRM [47]	For classifying the samples using thin section images.
Petrography	Folk [50], Dunham [51]	

**Figure 1.** Example samples for PWV, PLI, and UCS tests: (a) device for measuring PWV, (b) example samples after PLI test, and (c) sample under UCS test.

2.2. Random Forest Algorithm (RFA)

The random forest method is one of the ensemble methods. In these methods, the model chosen for classification or regression is a combination of several models. Figure 2

shows the idea of the random forest algorithm. In this approach, each model issues its vote and the final result about the value is issued based on these votes [22,23,52]. The general principles of group training techniques are based on the assumption that their accuracy is higher than other training algorithms [53]. On the other hand, the accuracy of combined methods is higher than the accuracy of its components [53]. The RFA method has also been used in rock mechanics in recent years [20]. In the RFA method, the models used in the combined method, which are all of the decision tree type, form a forest. Each of the decision trees is made using a random selection of special attributes in each node to determine the branching. In other words, each tree is built based on the values of a random vector. These values have the identical scattering for all trees in the forest and are sampled independently. For classification, each tree issues its vote, and the final result is determined by the majority vote [54]. The number of trees and the number of chosen variables in each node are important parameters in the RFA [55]. In this method, by replacing the information every sampling time, some information is never sampled, and other data may be sampled several times. In other words, some input data for some trees will be out of the bag, that is, they will not participate in the creation of some trees. These data have the function of an internal validator for each tree, which is performed by estimating the out-of-bag error. If the out-of-bag data itself is predicted through trees, there will be an error for these predictions, and the average of these errors is called the out-of-bag error. This error indicates the influence of the unselected samples on the error rate of the final result of the random forest [56].

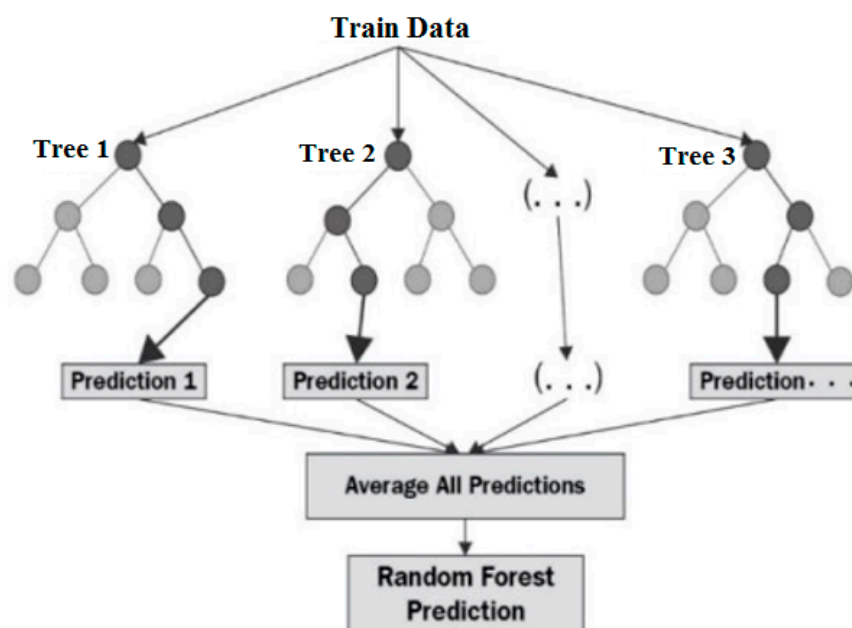


Figure 2. Concept of random forest algorithm.

2.3. Gaussian Process Regression Based on Squared Exponential Kernel (GPR-SEK)

Consider a d data set with n measurements: $d = \{(x_i, y_i) | i = 1, \dots, n\}$, where x_i is the input vector with D dimension and y_i is the target output. This set, consisting of two components, input and output, will be denoted as measured points. To simplify the problem, the inputs of the collection are aggregated at $X = \{x_1, x_2, \dots, x_n\}$ matrix and the outputs are also combined at $Y = \{y_1, y_2, \dots, y_n\}$ matrix. Regression based on the data set d creates a new input x^* to arrive at the predicted distribution for the corresponding values of the measured y^* data. The Gaussian process (GP) is a group of accidental parameters, a restricted number of which are combined with Gaussian distributions (GDs) [57]. The GP is a generalization of GD. The GD is actually scattered between accidental parameters,

while GP represents scattering between functions. The $f(x)$ GP is described using the $m(x)$ average and covariance functions according to Equations (1) and (2).

$$m(x) = E(f(x)) \quad (1)$$

$$c(x, x') = E(f(x) - m(x))(f(x') - m(x')) \quad (2)$$

In relationships 1 and 2, $c(x, x')$ is the covariance or kernel function, which is computed at the x and x' points. The GP can be described as Equation (3).

$$f(x) \sim GP(m(x), c(x, x')) \quad (3)$$

Usually, for simplification, the value of the average function is considered equal to zero [58]. In the GP, the correlation between the target and the input vector is based on Equation (4).

$$y_i = f(x_i) + \varepsilon \quad (4)$$

where $f(x_i)$ represents the arbitrary regression function and ε is the noise of the Gaussian function with zero mean and σ^2 variance (i.e., $\varepsilon \sim N(0, \sigma^2)$). Furthermore, it is supposed that $f = [f(x_1), f(x_2), \dots, f(x_n)]^T$ has a performance according to the GP (i.e., $p(f|X) = N(0, C)$). Here, C is the covariance matrix with the $c_{i,j} = c(x_i, x_j)$ domains.

$$C(X, X) = \begin{pmatrix} c(x_1, x_1) & c(x_1, x_2) & \dots & c(x_1, x_n) \\ c(x_2, x_1) & c(x_2, x_2) & \dots & c(x_2, x_n) \\ \vdots & \vdots & \ddots & \vdots \\ c(x_n, x_1) & c(x_n, x_2) & \dots & c(x_n, x_n) \end{pmatrix} \quad (5)$$

The $c_{i,j}$ is the covariance between the latent function values of $f(x_i)$ and $f(x_j)$. GP regression is used to calculate the predicted scattering for the f^* function values in the test points of $X^* = [x_1^*, x_2^* \dots x_m^*]$. The distribution of y depends on the values of f , which is represented by an isotropic Gaussian as follows.

$$p(y|f, x) = N(f, \sigma_n^2 I) \quad (6)$$

In relation (6), I is the identity matrix. According to the characteristics of the Gaussian function, the marginal distribution of y is determined as follows.

$$p(y|X) = \int p(y|f, X) p(f|X) df = N(0, C + \sigma_n^2 I) \quad (7)$$

The integrated distribution of the observation data values, that is, the desired output, and the function values at the test points are written as follows [32].

$$\begin{bmatrix} y \\ f^* \end{bmatrix} \sim N\left(0, \begin{bmatrix} C(X, X) + \sigma^2 I & C(X, X_*) \\ C(X_*, X) & C(X_*, X_*) \end{bmatrix}\right) \quad (8)$$

According to relation (3), and using standard rules to limit Gaussian, the following conditional distribution can be obtained.

$$p(f_*|X, y, X_*) \sim N(\bar{f}_*, c(f_*)) \quad (9)$$

$$\bar{f}_* = C(X_*, X) [C(C, C) + \sigma^2 I]^{-1} y \quad (10)$$

2.4. The SVM-RBF

To achieve the least error related to the test set, the SVM-RBF approach fits a linear line with epsilon (ϵ) thickness on the data [59]. In this method, a function such as $f(x) = m \cdot x + b$ is used for forecasting, where m is weight vector and x and b are weights.

For minimizing weight vector and test error, this technique utilizes error functions for ignoring errors that are at a determined range from the real errors [60]. Hence, some deviation (derived from Equation (11)) from ϵ must be overlooked by including Equation (11) in Equation (12), which considers the ξ_i^- and ξ_i^+ deficiency parameters. Finally, the error values are optimized via Equation (12) using structural error minimization

$$|\xi|_{\epsilon} = \begin{cases} 0 & \text{if } |\xi| \leq \epsilon \\ |\xi| - \epsilon & \text{otherwise} \end{cases} \quad (11)$$

$$\begin{aligned} \text{Minimize : } & \{(\|m\|^2) * 1/2\} + \{(\sum_{i=1}^N (\xi_i^+ + \xi_i^-)) * C\} \\ \epsilon \text{ Constrains : } & \begin{cases} m \cdot x_i + b + \xi_i^+ - y_i \leq \epsilon & i = 1, 2, \dots, N \\ y_i - (b + m \cdot x_i) \leq \xi_i^- + \epsilon & i = 1, 2, \dots, N \\ \xi_i^+ \geq 0, \xi_i^- \geq 0 & i = 1, 2, \dots, N \end{cases} \end{aligned} \quad (12)$$

In Equation (12), $\{(\|m\|^2) * 1/2\}$ is the supervisory part, N is number of samples, ϵ is the allowable error, C is the complexity balance coefficient, and the ϵ values are the acceptable error range. As with the GPR method, various kernel functions are used in the SVM method [61]. Radial basis function (RBF), which is the most important kernel function, was used in the current research [62].

2.5. K Nearest Neighbor Algorithm (KNN)

The KNN is based on sample and performs classification based on K nearest neighbors. This method performs classification based on the similarity of the data. In fact, for each new test data, it calculates the K nearest neighbor distances and determines a label similar to the dominant label of this k neighbor for the desired point [63]. This method was introduced as a nonparametric method and does not make any assumption on the distribution of inputs. Therefore, it is extensively used in various fields [64].

In the KNN classifier, an unknown value, is recognized by the similarity between known trained or labeled values based on the calculation of the distance between unknown values and labeled values. Then, K of the nearest values are selected as the basis for classification, and the unknown value (x test) is assigned to the class that has the most values among the closest values. For this purpose, three factors affect the KNN classification: (1) the number of K of the neighbor and the changing of the value of K, which may amend the classification results; (2) labeled dataset; therefore, adding or eliminating any value to the training samples affects the final results of the KNN classifier; (3) the distance criterion. In KNN, Euclidean distance is usually used as a distance criterion to measure the distance between two values [64,65]. This algorithm, as with the other algorithms used in this research, after examining the data in the program environment, divides the data into two parts, training data and test data, and builds the K nearest neighbor model and enters the training data into the model to train the model. Next, to determine the precision of the method, the test data is entered into the model for prediction and to evaluate the prediction accuracy in comparison with the labels of the test data [65,66].

2.6. ANFIS and FMP-ANN

The ANFIS and FMP-ANN methods have been widely introduced and described by previous researchers [18,25,67–70]. The transfer functions of neurons, membership functions, type of fuzzy inference system, and data training methods in these two methods are mentioned in the results section.

In the SVM-RBF, ANFIS, KNN, GPR-SEK, and RFA methods, 30% and 70% of the whole data were used for the testing and training the models, respectively.

2.7. Performance Evaluation of Results

To appraise the methods, the correlation coefficient, the MAPE %, the RMSE, VAF, and the PI are defined in the form of Equations (13)–(16).

$$\text{MAPE} = \frac{1}{n} \sum_{i=1}^n \left| \frac{y - y'}{y} \right| * 100 \quad (13)$$

$$\text{RMSE} = \frac{1}{s^2 n} \sum_{i=1}^n (y - y')^2 \quad (14)$$

$$\text{VAF} = 100 \left[1 - \frac{\text{var}(y - y')}{\text{var}(y)} \right] \quad (15)$$

$$\text{PI} = R^2 + (\text{VAF}/100) - \text{RMSE} \quad (16)$$

In relationships 13 to 16, y is the value of the variable measured, y' is the predicted UCS, and n is the total data and s^2 is the sample variance. Equation (17) was used to normalize the data between -1 and 1 .

$$X_i = 2 \left(\frac{X - X_{\min}}{X_{\max} - X_{\min}} \right) - 1 \quad (17)$$

In Equation (17), x is the measured variable, X_{\min} is the minimum of the data, and X_{\max} is the maximum of the data.

3. Results and Discussion

3.1. Geomechanical Properties of Samples

The maximum, minimum, and average engineering properties of 65 samples (37 samples of limestone, 11 samples of argillaceous limestone, and 17 samples of sandstone) are presented in Table 3. The average E_s and UCS are 14.95 GPa and 37.54 MPa, respectively. Physical, mineralogical, and petrographic characteristics cause changes in the compressive strength of rocks [5,18,71]. Moreover, lithological properties such as the type of rock, the amount and type of minerals, the type of cement between the particles that comprise the rock and physical properties such as the amount of moisture, porosity, and water absorption have a significant effect on the compressive strength and, consequently, on the stability of mines [72,73]. As the amount of clay minerals increases, the resistance of the samples decreases [4,74]. Water absorption causes the swelling and instability of the mine wall in samples with a high percentage of clay minerals [75–77]. The number of joints changes the geomechanical properties and instability of the rocky slopes [78–80]. The engineering properties and stability of structures are affected by the amount of moisture [81].

Table 3. Laboratory results on sample.

Properties Statistics	Density (g/cm ³)	PLI (MPa)	Water Absorption (%)	Porosity (%)	UCS (MPa)	E_s (GPa)	PWV (km/s)
Average	2.43	3.75	6.81	9.44	37.54	14.95	4.38
Std. Dev.	0.11	1.66	1.87	3.35	16.49	5.30	1.03
Kurtosis	0.13	(0.58)	(0.50)	(0.41)	(0.58)	(0.51)	(0.38)
Skewness	(0.42)	0.09	0.70	0.79	(0.71)	(0.62)	(0.78)
Min.	2.10	0.31	4.08	4.36	4.12	3.00	2.06
Max.	2.63	8.00	11.00	16.72	59.72	22.90	5.79
Specimens	65	65	65	65	65	65	65

In the sandstone samples of the present research, clay and gypsum were found. The cement of the samples is gypsum and calcite. The grains of these sandstones are semi-

rounded to angular and have a moderate to poor grading. The study of the thin sections of the samples showed that the samples with higher clay content show lower resistance characteristics. Swelling clay minerals (such as montmorillonite) were not observed in the investigated samples. Generally, rock bursting occurs in deep mines and in quartz-rich rocks [12]. Because the depth of the studied mines is less than 50 m and the overburden stress is negligible, the risks of rock bursting have not been reported in them so far.

3.2. Petrographic Features

Texture has a special effect on the engineering properties of sedimentary rocks [82]. In carbonates, the rock texture is very different, but their mineralogy is not much different [83,84]. According to microscopic studies, the most basic mineral of limestone rocks was calcite. Mishan formation limestone rocks, with an early Miocene age, based on the Dunham [51] classification, were classified in the range of mudstone to grainstone. Moreover, argillaceous limestone samples of this formation were classified in the mudstone to packstone categories. Sandstone samples of the Aghajari formation with an upper miocene age were classified as calc-litharenite according to the Folk [50] classification. These rocks consist of carbonaceous rock fragments (26 to 75%), volcanic gravel (2 to 35%), meta-morphic fragments (2 to 18%), feldspar (1 to 10%), dark minerals (1 to 8%), quartz (0 to 22%), and chert (2 to 11%).

3.3. Influence of Independent Variables on the UCS

Figure 3 shows the effect of variables on the UCS. There is a reasonable tendency among these characteristics. The UCS decreases with increasing WW and porosity. This Figure shows that porosity has the highest effect on the UCS. Numerous studies have reported linear relationships with high accuracy between the point load index (PLI) and UCS [8,30]. The results of the relationship between PVW and UCS show that PVW displays a high accuracy to estimate UCS (Figure 3).

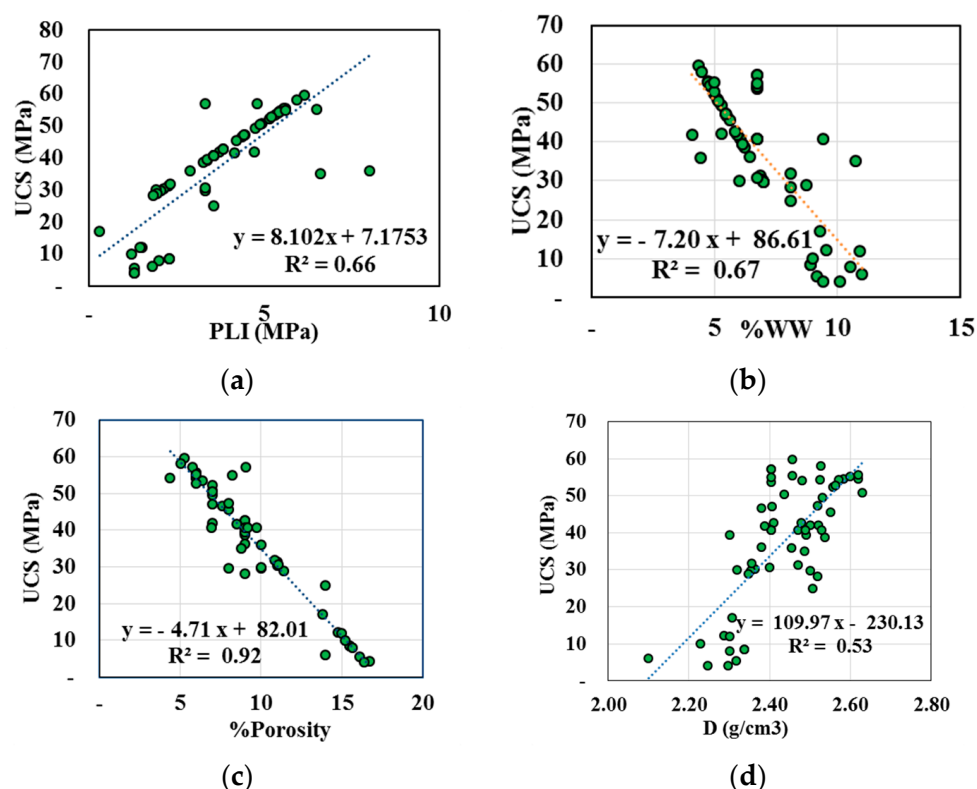


Figure 3. Cont.

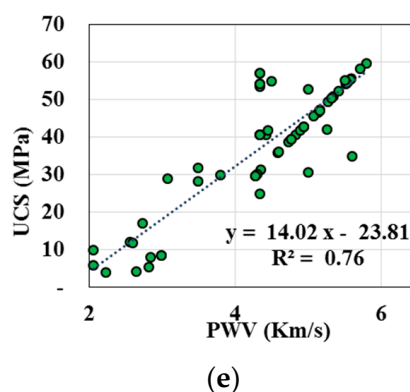


Figure 3. Effect of (a) point load index (PLI), (b) water absorption by weight (WW), (c) %porosity, (d) density (D), and (e) P–wave velocity (PWV) on the UCS.

3.4. Evaluation of Previous Empirical Relationships

For predicting the UCS of the rocks, some empirical relationships have been proposed (Table 1). In the current research, for each of the 65 samples of the present study, based on each of the empirical relationships in Table 1, UCS was predicted. Finally, the accuracy of the forecasted and actual UCS relationships were assessed.

Figure 4 displays the data scattering and the precision of correlation using PI and R^2 . The results revealed that there is good compatibility between actual UCS and the estimated one using previous studies (Figure 4). A performance index (PI) was introduced by Yagiz et al. [85] for evaluating empirical equations and models. The value of this index is equal to two in the best case, and the lower it is, the lower the relationship performance. As can be seen, although the correlation coefficient is high, the performance index is negative, which indicates the poor performance of the previous researchers' relationships in estimating the UCS of the studied rocks (Figure 4). For this reason, various researchers have emphasized that empirical relationships should be determined for each region [85].

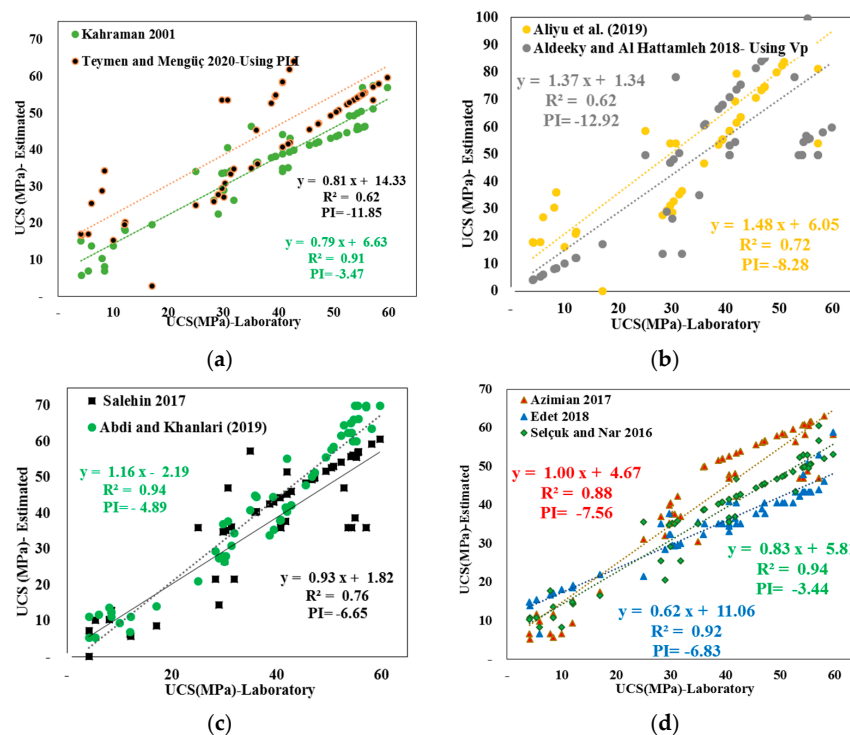


Figure 4. Measured UCS versus predicted UCS based on relationships of (a) Kahraman [43] and Teymen and Mengüç [40], (b) Aliyu et al. [30], Aldeeky and Al Hattamleh [42], (c) Salehin [41], Abdi and Khanlari [4], (d) Azimian [29], Edet [3], and Selcuk and Nar [31].

The type of rock, strength amount, method of conducting experiments, the test conditions (such as loading rate), and the petrography of the specimens of a specific study reveal the applicability of the proposed relationships for forecasting the UCS of rocks in other regions. For example, the average UCS of the samples of Edet [3] study was 32.22 MPa, and the average UCS of the present study is 37.54 MPa, which shows that the resistance of the Edet [3] study samples is lower than the resistance of the current research samples. As a result, the UCS values estimated from this researcher's relationship are mostly below the diagonal line (Figure 4d). The sample breaks faster and shows more resistance when the loading rate is increased.

3.5. Multiple Linear Regression (MPLR)

In the current work, MPLR analysis was performed using Minitab software (version 18). Equation (18) was developed to predict the UCS using this method. Various criteria to evaluate this relationship are presented below.

Various statistics (Tables 4 and 5) were used to evaluate relationship 18. The Durbin–Watson statistic (DWS) and variance inflation factor (VIF) are used to evaluate the independence of errors and the correlation of independent variables, respectively [86]. The results showed that there is no problem in using relationships in terms of these two criteria because the DW is in the range of 1.5 to 2 and the VIF value is less than 10 (Table 5). Analysis of variance (ANOVA) results (Sig. < 0.00) show that the model has been well developed using MPLR. Sig. values (related to T-test) in Table 5 indicate the presence of variables in the multivariate regression output relationship. The constant value, density, and water absorption were removed from Equation (18) because the sig. value is more than 0.05.

Table 4. Multiple linear regression results to estimate UCS and Es.

Equation	R ²	RMSE (MPa)	MAPE%	VAF %	PI	DWS	ANOVA Results	Eq. No.
UCS = 5.03PWV − 1.735φ + 2.667PLI	0.88	1.10	1.08	87.85	0.66	1.93	F-value = 79.37 p-value = 0.00	(18)

Table 5. Evaluation criteria of coefficients for relationship 18.

Term	Coefficients	T-Value	Significant Level (Sig.)	VIF (Variance Inflation Factor)
Constant	−32.1	−1.34	0.187	–
PWV	5.03	2.44	0.018	7.58
D	21.4	1.82	0.074	3.02
WW	0.281	0.35	0.728	3.81
φ	−1.735	−3.97	0.000	3.64
PLI	2.667	3.05	0.003	3.77

The normality of the error distribution is also one of the other criteria for evaluating empirical relationships. The normal distribution of errors related to the model provided by MPLR method shows that the proposed model can be used to estimate UCS (Figure 5).

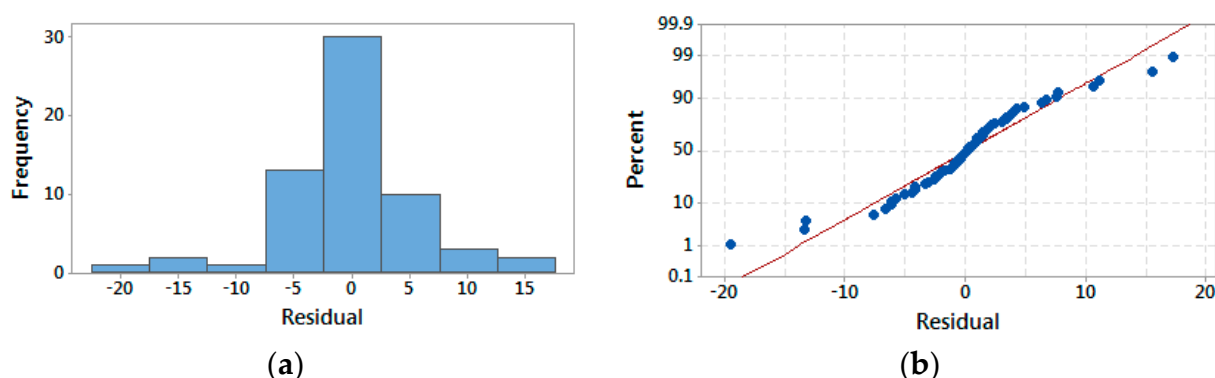


Figure 5. Normal state of the residues of model 18 (a) histogram of residuals, and (b) normal probability plot.

3.6. The Results of Modeling Using RFA and GPR-SEK Methods

The RFA modeling was conducted using the R (version R4.2.1) software [54]. The GPR-SEK model was conducted using MATLAB software (MATLAB 2016b). In the RF method, the 10-fold cross-validation method was used to control the number of chosen parameters in each node of tree (m-try) and the number of trees (n-tree). According to this method, the number of 500 trees and five variables in each node has delivered the most satisfactory conditions for modeling. Therefore, these values were used for modeling purposes.

The random forest method works well for large amounts of data and has high accuracy. In the random forest method, because the amount of error decreases with the increase of trees, 500 trees were used to develop the model. Upon model execution, the results were evaluated using an out-of-bag (OOB) error estimation. The model was appraised by the test data, the results of which are presented in Figure 6. One of the advantages of the random forest algorithm is that it can determine the importance of variables in a problem. In this research, the significance of the inputs was achieved using the Gini significance index [54]. The results showed that porosity has higher importance than other parameters. In Figure 6, the error histogram, the graph of the measured, the forecasted UCS using the RFA method, and the GPR-SEK model are drawn. The GPR-SEK model was implemented based on the squared exponential kernel function. As can be seen in the figure, the results are close to the bisector line, and it can be said that the values have been predicted with good accuracy. Theoretically, if R^2 equals 100%, all the observed values will be similar to the fitted values and all the data points will be on the fitted line [87].

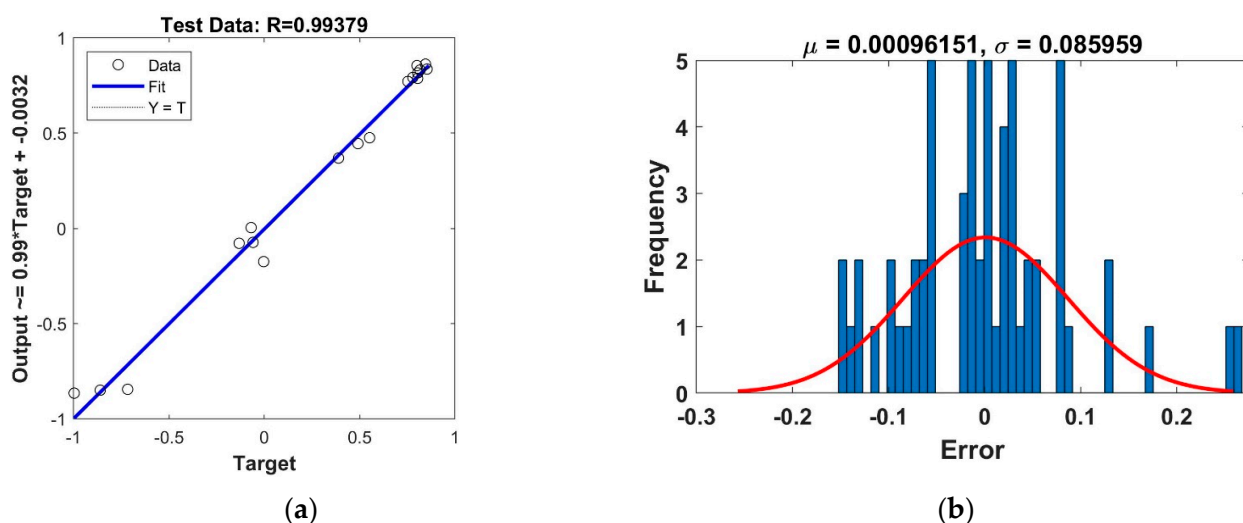
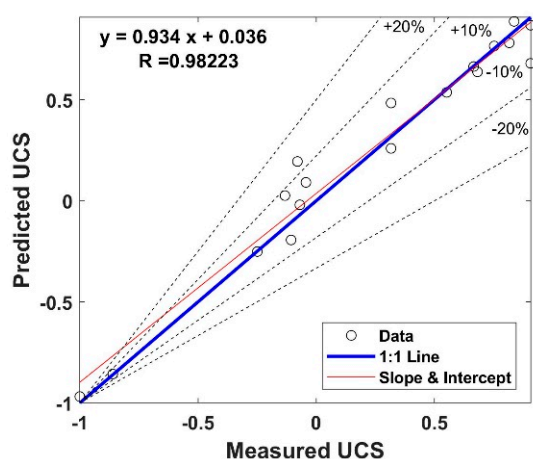
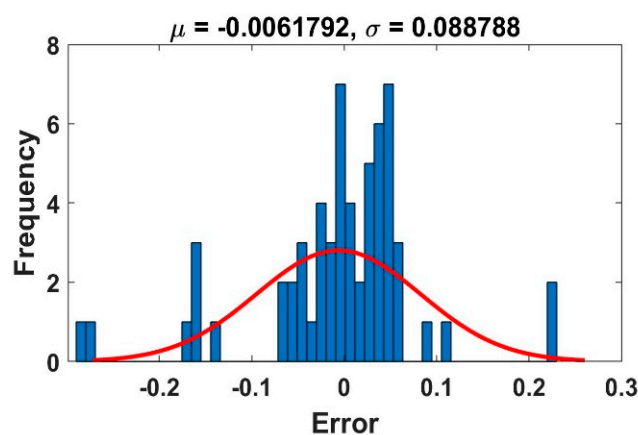


Figure 6. Cont.



(c)



(d)

Figure 6. Results of (a) RFA for test data, (b) RFA for all data, (c) GPR-SEK for test data, and (d) GPR-SEK for all data.

3.7. The FMP-ANN Results

The FMP-ANN is widely used in engineering [88,89]. In the current study, for predicting UCS, various neurons in a hidden layer were investigated to develop optimal models. Based on equations proposed by previous researchers, the number of hidden layer neurons changes were determined (Table 6). The calculated number of hidden layer neurons changed from one to eleven according to Table 6. In this study, by checking this range using the FMP-ANN, this range was evaluated to achieve the ideal model architecture for forecasting UCS.

Table 6. Proposed equations by previous researchers to estimate the number of hidden layer neurons.

References	Neuron Numbers Calculated for This Study	Equations
Hecht-Nielsen [90]	≤ 3	$\leq 2 * N_i + 1$
Hush [91]	3	$3N_i$
Ripley [92]	3	$(N_i + N_0)/2$
Paola [93]	11	$\frac{2 + N_i * N_0 + 0.5N_0 * (N_0^2 + N_i) - 3}{(N_i + N_0)}$
Wang [94]	1	$2N_i/3$
Kaastra and Boyd [95]	2	$\sqrt{N_0 * N_i}$
Kanellopoulos and Wilkinson [96]	1	$2N_i$

N_0 and N_i are the numbers of input and output neurons, respectively.

The used FMP-ANN method has a hidden layer with five inputs (PWV, point load index (PLI), porosity, density, and water absorption) and one output (UCS). Using MATLAB software, the Levenberg Marquardt (LM) training algorithm was used to train the network. The neuron transfer functions were the selected Sigmoid between the input layers and hidden layers and the Purelin between the hidden layers and output layers. In FMP-ANN modeling, the percentages of the validation, test, and training data in the present study were randomly selected as 15%, 15%, and 70% of the total data, respectively. The validation set is used to prevent overfitting, the training group is used to determine weights, and the test group is used to evaluate the FMP-ANN results [97–100]. The results showed that the third neuron is the most accurate neuron for estimating UCS. Figure 7 displays the optimal FMP-ANN chart achieved in the current research.

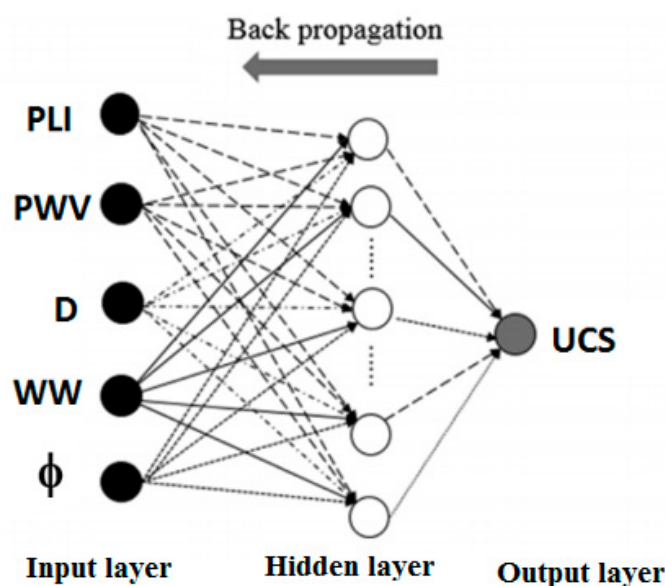


Figure 7. Used FMP-ANN structure.

Figure 8 shows the error variations in optimum results. The lowest error in epoch 4 was obtained for predicting the UCS (Figure 8). Moreover, in this research, the results of the FMP-ANN to estimate UCS have been compared with several methods. It was found that the accuracy of all methods was very high (the coefficient of determination is more than 97%).

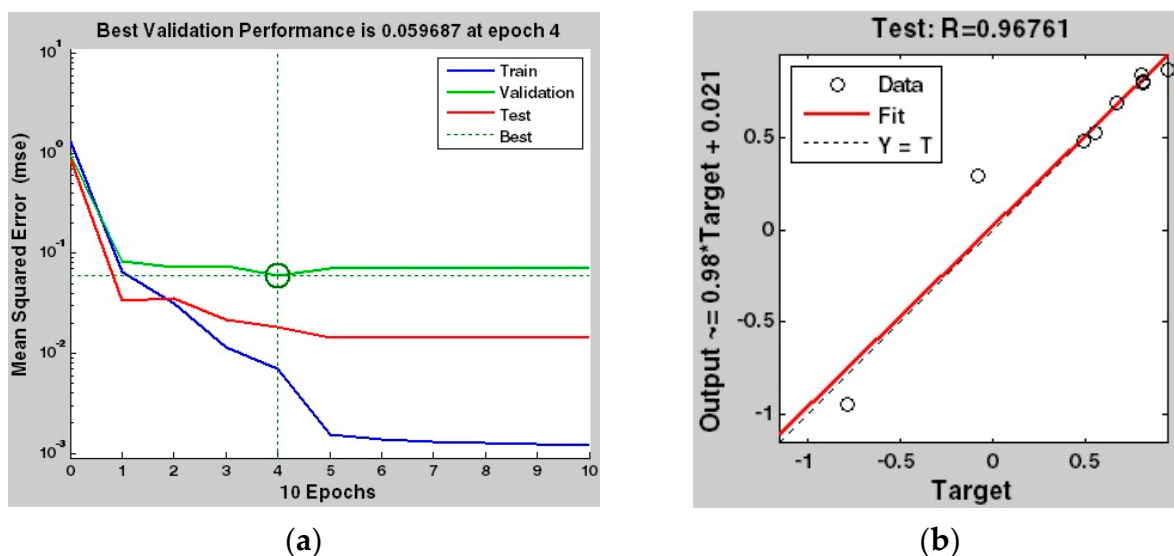


Figure 8. The FMP-ANN results for the optimum model (a) error reduction trend and (b) correlation coefficient between measured and predicted UCS.

3.8. The KNN Results

To apply the KNN method to the data and determine the best K value, the KNN was written in the form of a program in MATLAB software, which was run 310 times for K values from 1 to 30 programs; moreover, the amount of error was measured (Figure 9). Of the total data, 70% and 30% were used to train and test the model. The results showed that the lowest estimation error of the UCS was obtained at $K = 2$ (Figure 9). The error of this network for estimating the UCS with respect to the K values is equal to 0.11 (Figure 10). Figure 10 shows the KNN results for estimating the UCS.

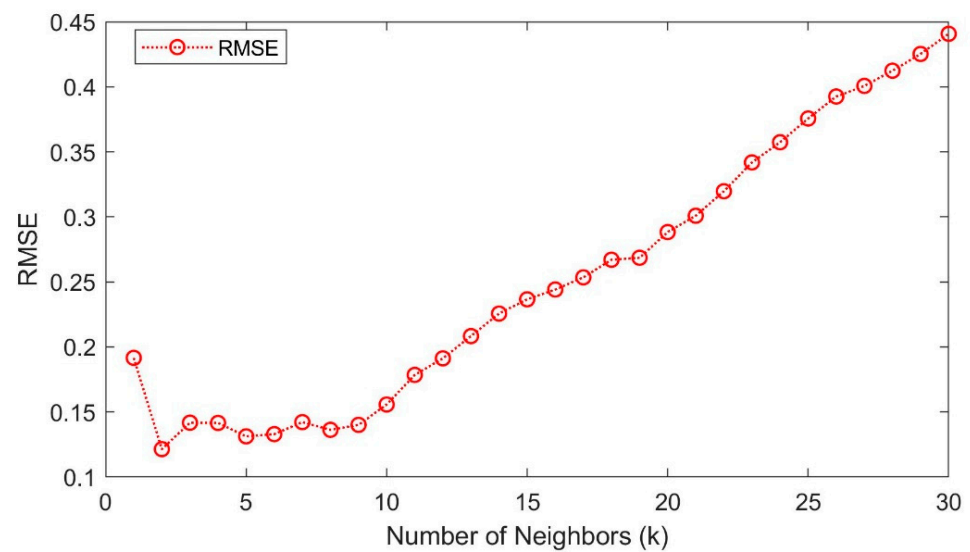


Figure 9. Obtained RMSE for forecasting UCS based on the KNN for different values of K.

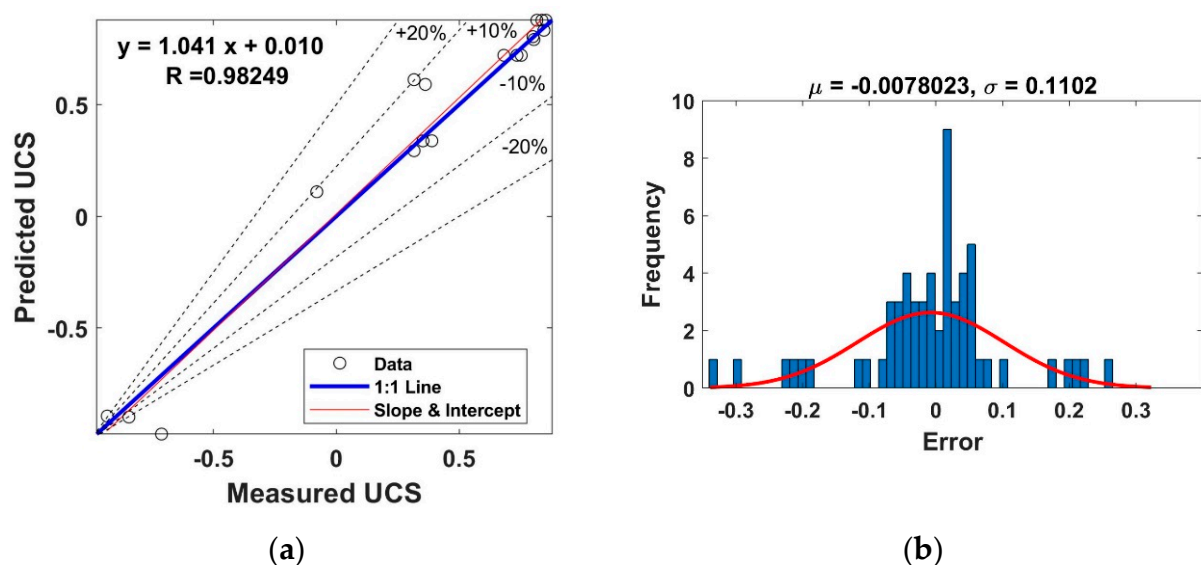


Figure 10. Accuracy of predicted UCS using KNN: (a) correlation coefficient for test data and (b) error histogram for all data.

3.9. Results of SVM Method for Estimating UCS

The SVM algorithm uses a set of mathematical functions that are named kernels [101]. The most important kernel functions for solving engineering problems are listed in Table 7. Normally, three radial basis kernel functions (RBFs), polynomial of degree, d , and linear, are used in the support vector machine, and the use of each of these functions with different parameters in the estimation of rock strength may lead to different results [60,101]. Therefore, it is necessary to evaluate the efficiency and accuracy of each of these functions and to choose the appropriate kernel function in predicting resistance. These three kernel functions were also used in this research. It should be mentioned that the calculation process of SVM was performed based on coding in a MATLAB environment and that the parameters of the kernel functions were optimized using a trial and error process. The results of these investigations are presented in Table 8. It can be observed that, based on the statistical criteria, the accuracy of the kernel functions is as $RBF > PK > LK$. In this regard, Nguyen [102] investigated the performance of various kernel functions using the support

vector machine method in estimating blast-induced ground vibration and stated that the radial basis function has the highest performance.

Table 7. The most important kernel functions for solving engineering problems [102].

Function	Description	Kernel Function Type
$k(x_i, x_j) = (x_i \cdot x_j + 1)^d$	This kernel is widely used in image processing, where d is the degree of the polynomial.	Polynomial kernel (PK)
$k(x_i, x_j) = \exp(-\gamma \ x_i - x_j\ ^2)$	This kernel is used for general purposes. It is used when there is no prior knowledge about the data. In $\gamma > 0$ condition, $\gamma = 1/2\sigma^2$ parameter is used.	Radial basis function (RBF)
$k(x_i, x_j) = x_i \cdot x_j$	-	Linear kernel (LK)

Table 8. Evaluation of SVM model performance in UCS estimation using various kernel functions.

Kernel Function	Optimal Values of Parameters					Test Period				Train Period			
	ϵ	t	d	σ	c	RMSE	R^2	PI	MAPE	RMSE	R^2	PI	MAPE
PK	1.72	280.01	4	-	12.12	0.08	0.97	1.87	2.86	0.07	0.98	1.84	2.81
RBF	0.02	-	-	1.10	27	0.06	0.99	1.90	2.82	0.06	0.99	1.90	2.80
LK	0.45	-	-	-	0.90	0.09	0.96	1.83	2.84	0.09	0.97	1.81	

The error histogram and predicted and estimated UCS relationship with the optimal function (RBF function) are presented in Figure 11.

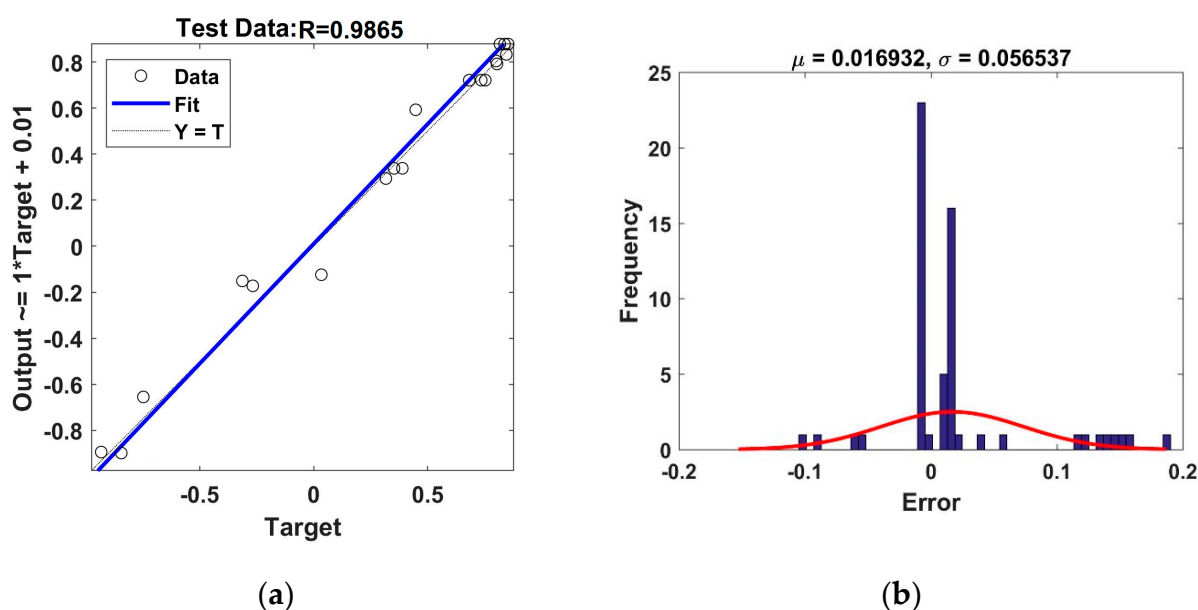


Figure 11. Accuracy of predicted UCS using SVM-RBF: (a) correlation coefficient and (b) error histogram for all data.

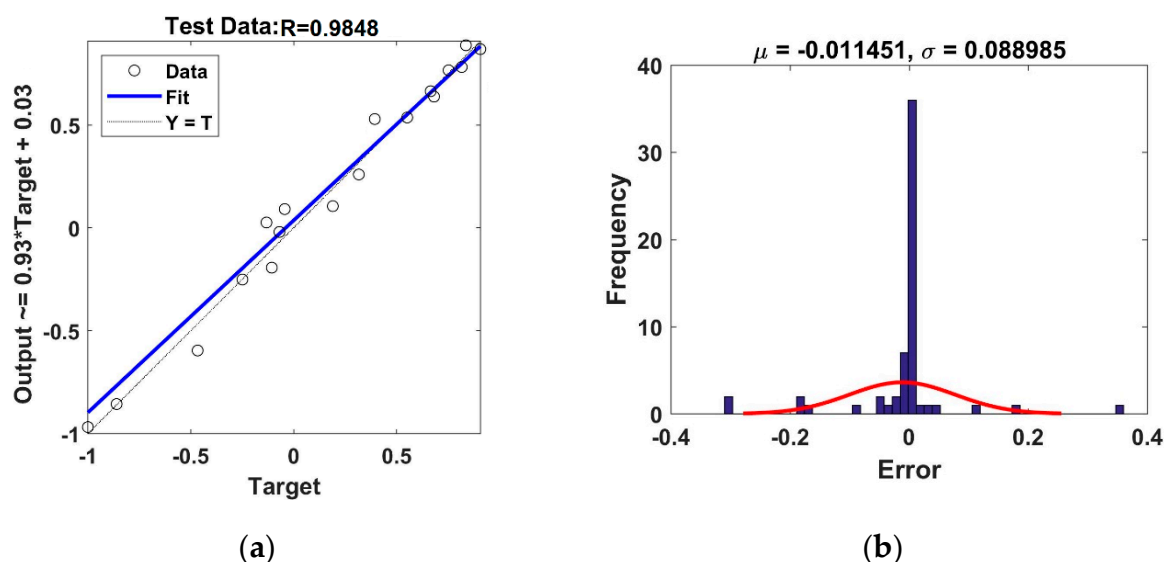
3.10. Results of ANFIS Method for Estimating UCS

As with other intelligent methods, to test and train models using ANFIS, 30% and 70% of the whole data were used, respectively. The method of combining regression error propagation with least squares was used to train the model using the ANFIS. Table 9 shows the modeling features using the ANFIS method. A comparison of the performance of the methods for forecasting UCS based on different criteria has been reported in the next section.

Table 9. Modeling features using ANFIS.

FIS Generation Method	GENFIS4
Influence radius	0.60
Number of epochs	500
Error goal	0.00
Type	Sugeno
Rules	4
Number of membership functions (MFs)	6
Input MF type	Gauss MF
Output MF type	Linear

Figure 12 shows the error histogram and correlation coefficient of the ANFIS model in the test stage. This method, as with other used intelligent methods, has high accuracy in UCS estimation. The results of the intelligent models for estimating UCS from the test data performed better than the training data; therefore, it can be argued that overfitting did not occur.

**Figure 12.** Accuracy of predicted UCS using ANFIS: (a) correlation coefficient and (b) error histogram for all data.

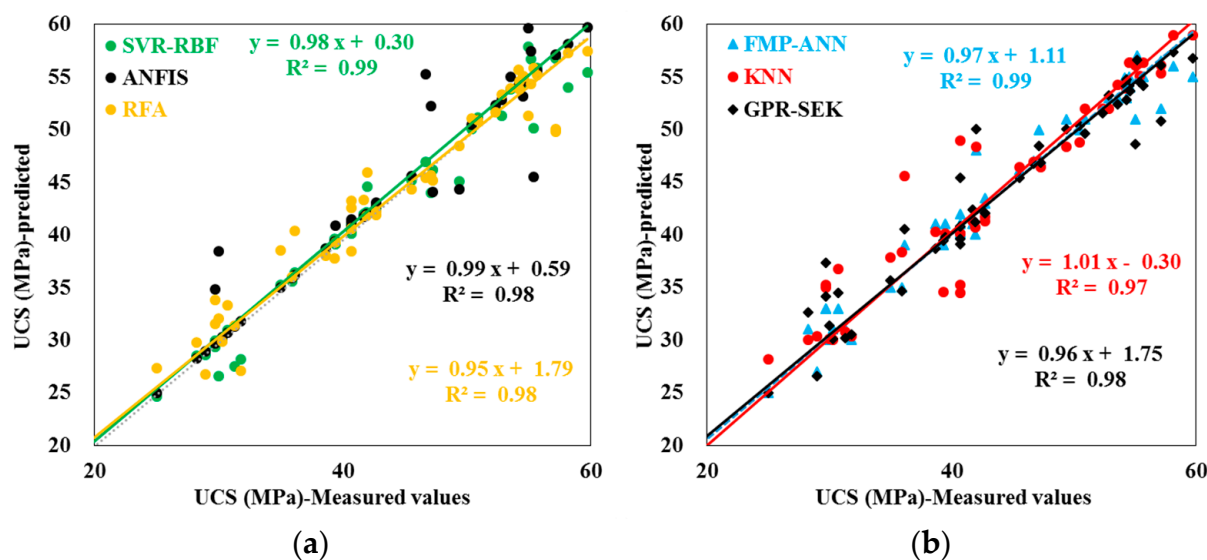
3.11. Evaluation of the Used Methods

Table 10 and Figure 13 show the accuracy of the used methods for forecasting the UCS. According to the statistical criteria (i.e., R^2 , MAPE%, RMSE, VAF, and PI), the SVM-RBF model displays greater precision than other models because the SVM uses the minimizing structural risk theorem and adapts the ability of the model to existing training data [103]. The number of input variables, number of samples, and training algorithm type also affect the accuracy of the methods [16,104,105]. Based on the correlation coefficient, all methods ($R^2 > 90\%$) have excellent accuracy for estimating UCS.

Considering that all six intelligent methods showed very high accuracy in UCS estimation, the percentage difference of the average of all six intelligent methods with the measured value in the laboratory is equal to +0.28%. This amount of difference is less than 1% and indicates the high capability of intelligent methods for forecasting the UCS.

Table 10. Accuracy of approaches for predicting UCS.

APPROACHES	MAPE%	R ²	RMSE	VAF%	PI
RFA	9.27	0.98	0.09	97.63	1.87
SVM-RBF	2.83	0.99	0.06	98.96	1.92
ANFIS	2.98	0.98	0.09	97.86	1.87
KNNA	8.44	0.97	0.11	97.25	1.83
GPR-SEK	6.63	0.98	0.09	97.45	1.86
FMP-ANN	4.66	0.99	0.24	98.36	1.73

**Figure 13.** Measured values versus predicted UCS using (a) SVR–RBF, ANFIS, and RFA methods, and (b) FMP–ANN, KNN, and GPR–SEK methods.

4. Conclusions

The UCS of rocks is a basic parameter necessary for assessing the construction of civil and mining structures, such as the stability of the mines and the bearing capacity of foundations. UCS estimation using core specimens is costly, difficult, and, in some cases, impossible. After assessing the geo-mechanical features of 55 samples of sandstone, limestone, and argillaceous limestone specimens, predictive models for estimating UCS were developed via intelligent and statistical approaches. The results showed that the carbonate and sandstone samples were classified as mudstone to grainstone and calc-litharenite, respectively. The PWV, WW, porosity, density, and PLI were considered as model inputs for predicting UCS. Statistical analysis allowed the development of equations with high accuracy to estimate UCS. Among the assessed linear, polynomial, and radial basis kernel functions, the accuracy of the other models was lower than that of SVM-RBF in forecasting UCS. The SVM-RBF model revealed that the R² and PI values were 0.99 and 1.92, respectively. The R² values of 98%, 98%, 97%, 98%, and 99% for forecasting the UCS were achieved using ANFIS, RFA, KNNA, GPR, and FMP-ANN, respectively. The number of samples and input variables had a significant impact on the performance of the methods. When the number of samples was small, the SVM method was more accurate. The percentage difference of the average of all six intelligent methods with the measured value was less than 1%, which indicates the superior capability of the intelligent methods in forecasting UCS.

Author Contributions: X.Z.: methodology, software, data curation. F.M.A.A.: Conceptualization, investigation. T.A.S.G.: writing—original draft preparation, methodology. A.H.D.A.-K.: analysis of results, validation. A.I.: performing field investigations and collecting samples R.B.Y.S.: writing—original draft preparation, resources. M.L.N.: supervision, project administration, funding acquisition. All authors have read and agreed to the published version of the manuscript.

Funding: This research received no external funding.

Institutional Review Board Statement: Not applicable.

Informed Consent Statement: The authors are fully aware and satisfied with the contents of the article.

Data Availability Statement: The data used in this study has been appropriately described in the manuscript.

Conflicts of Interest: The authors declare that they have no conflict of interest.

References

1. Yang, H.Q.; Zeng, Y.Y.; Lan, Y.F.; Zhou, X.P. Analysis of the excavation damaged zone around a tunnel accounting for geo-stress and unloading. *Int. J. Rock Mech. Min. Sci.* **2014**, *69*, 59–66. [\[CrossRef\]](#)
2. Yang, H.Q.; Xing, S.G.; Wang, Q.; Li, Z. Model test on the entrainment phenomenon and energy conversion mechanism of flow-like landslides. *Eng. Geol.* **2018**, *239*, 119–125. [\[CrossRef\]](#)
3. Edet, A. Correlation between Physico-mechanical Parameters and Geotechnical Evaluations of Some Sandstones along the Calabar/Odukpani-Ikom-Ogoja Highway Transect, Southeastern Nigeria. *Geotech. Geol. Eng.* **2018**, *36*, 135–149. [\[CrossRef\]](#)
4. Abdi, Y.; Khanlari, G.R. Estimation of mechanical properties of sandstones using P-wave velocity and Schmidt hardness. *New Find. Appl. Geol.* **2019**, *13*, 33–47.
5. Ajalloeian, R.; Mansouri, H.; Baradaran, E. Some carbonate rock texture effects on mechanical behavior, based on Koohrang tunnel data, Iran. *Bull. Eng. Geol. Environ.* **2017**, *76*, 295–307. [\[CrossRef\]](#)
6. Madhubabu, N.; Singh, P.K.; Kainthola, A.; Mahanta, B.; Tripathy, A.; Singh, T.N. Prediction of compressive strength and elastic modulus of carbonate rocks. *Measurement* **2016**, *88*, 202–213. [\[CrossRef\]](#)
7. Wen, L.; Luo, Z.Q.; Yang, S.J.; Guang, Y.Q.; Wang, W. Correlation of Geo-Mechanics Parameters with Uniaxial Compressive Strength and P-Wave Velocity on Dolomitic Limestone Using a Statistical Method. *Geotech. Geol. Eng.* **2018**, *37*, 1079–1094. [\[CrossRef\]](#)
8. Aladejare, A.E. Evaluation of empirical estimation of uniaxial compressive strength of rock using measurements from index and physical tests. *J. Rock Mech. Geotech. Eng.* **2020**, *12*, 256–268. [\[CrossRef\]](#)
9. Lawal, A.I.; Kwon, S.; Aladejare, A.E.; Oniyide, G.O. Prediction of the static and dynamic mechanical properties of sedimentary rock using soft computing methods. *Geomech. Eng.* **2022**, *28*, 313–324.
10. Lawal, A.I.; Olajuyi, S.I.; Kwon, S.; Aladejare, A.E.; Edo, T.M. Prediction of blast-induced ground vibration using GPR and blast-design parameters optimization based on novel grey-wolf optimization algorithm. *Acta Geophys.* **2021**, *69*, 1313–1324. [\[CrossRef\]](#)
11. Momeni, E.; Dowlatshahi, M.B.; Omidinasab, F.; Maizir, H.; Armaghani, D.J. Gaussian process regression technique to estimate the pile bearing capacity. *Arab. J. Sci. Eng.* **2020**, *45*, 8255–8267. [\[CrossRef\]](#)
12. Gao, W.; Karbasi, M.; Hasanipanah, M.; Zhang, X.; Guo, J. Developing GPR model for forecasting the rock fragmentation in surface mines. *Eng. Comput.* **2018**, *34*, 339–345. [\[CrossRef\]](#)
13. Dao, D.V.; Adeli, H.; Ly, H.B.; Le, L.M.; Le, V.M.; Le, T.T.; Pham, B.T. A sensitivity and robustness analysis of GPR and ANN for high-performance concrete compressive strength prediction using a Monte Carlo simulation. *Sustainability* **2020**, *12*, 830. [\[CrossRef\]](#)
14. Barham, W.S.; Rabab'ah Aldeeky, S.R.; Al Hattamleh, O.H. Mechanical and Physical Based Artificial Neural Network Models for the Prediction of the Unconfined Compressive Strength of Rock. *Geotech. Geol. Eng.* **2020**, *38*, 4779–4792. [\[CrossRef\]](#)
15. Armaghani, D.J.; Mamou, A.; Maraveas, C.; Roussis, P.C.; Siorikis, V.G.; Skentou, A.D.; Asteris, P.G. Predicting the unconfined compressive strength of granite using only two non-destructive test indexes. *Geomech. Eng.* **2021**, *25*, 317–330.
16. Kwak, N.S.; Ko, T.Y. Machine learning-based regression analysis for estimating Cerchar abrasivity index. *Geomech. Eng.* **2022**, *29*, 219–228.
17. Gül, E.; Ozdemir, E.; Sarıcı, D.E. Modeling uniaxial compressive strength of some rocks from turkey using soft computing techniques. *Measurement* **2021**, *171*, 108781. [\[CrossRef\]](#)
18. Alizadeh, S.M.; Iraj, A.; Tabasi, S.; Ahmed, A.A.A.; Motahari, M.R. Estimation of dynamic properties of sandstones based on index properties using artificial neural network and multivariate linear regression methods. *Acta Geophys.* **2022**, *70*, 225–242. [\[CrossRef\]](#)
19. Rastegarnia, A.; Teshniz, E.S.; Hosseini, S.; Shamsi, H.; Etemadifar, M. Estimation of punch strength index and static properties of sedimentary rocks using neural networks in south west of Iran. *Measurement* **2018**, *128*, 464–478. [\[CrossRef\]](#)

20. McElroy, P.D.; Bibang, H.; Emadi, H.; Kocoglu, Y.; Hussain, A.; Watson, M.C. Artificial neural network (ANN) approach to predict unconfined compressive strength (UCS) of oil and gas well cement reinforced with nanoparticles. *J. Nat. Gas Sci. Eng.* **2021**, *88*, 103816. [[CrossRef](#)]
21. Wang, M.; Wan, W.; Zhao, Y. Prediction of the uniaxial compressive strength of rocks from simple index tests using a random forest predictive model. *C. R. Méc.* **2020**, *348*, 3–32. [[CrossRef](#)]
22. Matin, S.S.; Farahzadi, L.; Makaremi, S.; Chelgani, S.C.; Sattari, G.H. Variable selection and prediction of uniaxial compressive strength and modulus of elasticity by random forest. *Appl. Soft Comput.* **2018**, *70*, 980–987. [[CrossRef](#)]
23. Gamal, H.; Alsaihati, A.; Elkatatny, S.; Haidary, S.; Abdurraheem, A. Rock strength prediction in real-time while drilling employing random forest and functional network techniques. *J. Energy Resour. Technol.* **2021**, *143*, 093004. [[CrossRef](#)]
24. Umrao, R.K.; Sharma, L.K.; Singh, R.; Singh, T.N. Determination of strength and modulus of elasticity of heterogenous sedimentary rocks: An ANFIS predictive technique. *Measurement* **2018**, *126*, 194–201. [[CrossRef](#)]
25. Hudaverdi, T. Prediction of flyrock throw distance in quarries by variable selection procedures and ANFIS modelling technique. *Environ. Earth Sci.* **2022**, *81*, 281. [[CrossRef](#)]
26. Yesiloglu-Gultekin, N.; Gokceoglu, C.; Sezer, E.A. Prediction of uniaxial compressive strength of granitic rocks by various nonlinear tools and comparison of their performances. *Int. J. Rock Mech. Min. Sci.* **2013**, *62*, 113–122. [[CrossRef](#)]
27. Yesiloglu-Gultekin, N.; Gokceoglu, C.A. Comparison Among Some Non-linear Prediction Tools on Indirect Determination of Uniaxial Compressive Strength and Modulus of Elasticity of Basalt. *J. Nondestruct. Eval.* **2022**, *41*, 10. [[CrossRef](#)]
28. Fathipour-Azar, H. Machine learning-assisted distinct element model calibration: ANFIS, SVM, GPR, and MARS approaches. *Acta Geotech.* **2022**, *17*, 1207–1217. [[CrossRef](#)]
29. Azimian, A. Application of statistical methods for predicting uniaxial compressive strength of limestone rocks using nondestructive tests. *Acta Geotech.* **2017**, *12*, 321–333. [[CrossRef](#)]
30. Aliyu, M.M.; Shang, J.; Murphy, W.; Lawrence, J.A.; Collier, R.; Kong, F.; Zhao, Z. Assessing the uniaxial compressive strength of extremely hard cryptocrystalline flint. *Int. J. Rock Mech. Min. Sci.* **2019**, *113*, 310–321. [[CrossRef](#)]
31. Selçuk, L.; Nar, A. Prediction of uniaxial compressive strength of intact rocks using ultrasonic pulse velocity and rebound-hammer number. *Q. J. Eng. Geol. Hydrogeol.* **2016**, *49*, 67–75. [[CrossRef](#)]
32. Mahmoodzadeh, A.; Mohammadi, M.; Ali, H.F.H.; Abdulhamid, S.N.; Ibrahim, H.H.; Noori, K.M.G. Dynamic prediction models of rock quality designation in tunneling projects. *Transp. Geotech.* **2021**, *27*, 100497.
33. Xu, C.; Amar, M.N.; Ghriga, M.A.; Ouaer, H.; Zhang, X.; Hasanipanah, M. Evolving support vector regression using Grey Wolf optimization; forecasting the geomechanical properties of rock. *Eng. Comput.* **2020**, *38*, 1819–1833. [[CrossRef](#)]
34. Ceryan, N. Application of support vector machines and relevance vector machines in predicting uniaxial compressive strength of volcanic rocks. *J. Afr. Earth Sci.* **2014**, *100*, 634–644. [[CrossRef](#)]
35. Trott, M.; Matthew, L.; Lindsay, H.; Daniel, L.M. Random forest rock type classification with integration of geochemical and photographic data. *Appl. Comput. Geosci.* **2022**, *15*, 100090. [[CrossRef](#)]
36. Barzegar, R.; Sattarpour, M.; Nikudel, M.R.; Moghaddam, A.A. Comparative evaluation of artificial intelligence models for prediction of uniaxial compressive strength of travertine rocks, case study: Azarshahr area, NW Iran. *Model. Earth Syst. Environ.* **2016**, *2*, 76. [[CrossRef](#)]
37. Mohamad, E.T.; Armaghani, D.J.; Momeni, E.; Abad, S. Prediction of the unconfined compressive strength of soft rocks: A PSO-based ANN approach. *Bull. Eng. Geol. Environ.* **2015**, *74*, 745–757. [[CrossRef](#)]
38. Singh, R.; Umrao, R.K.; Ahmad, M.; Ansari, M.K.; Sharma, L.K.; Singh, T.N. Prediction of geomechanical parameters using soft computing and multiple regression approach. *Measurement* **2017**, *99*, 108–119. [[CrossRef](#)]
39. Kaloop, M.R.; Bardhan, A.; Samui, P.; Hu, J.W.; Zarzoura, F. Computational intelligence approaches for estimating the unconfined compressive strength of rocks. *Arab. J. Geosci.* **2023**, *16*, 37. [[CrossRef](#)]
40. Teymen, A.; Mengüç, E.C. Comparative evaluation of different statistical tools for the prediction of uniaxial compressive strength of rocks. *Int. J. Min. Sci. Technol.* **2020**, *30*, 785–797. [[CrossRef](#)]
41. Salehin, S. Investigation into engineering parameters of marls from Seydoon dam in Iran. *J. Rock Mech. Geotech. Eng.* **2017**, *9*, 912–923. [[CrossRef](#)]
42. Aldeeky, H.; Al Hattamleh, O. Prediction of engineering properties of basalt rock in Jordan using ultrasonic pulse velocity test. *Geotech. Geol. Eng.* **2018**, *36*, 3511–3525. [[CrossRef](#)]
43. Kahraman, S. Evaluation of simple methods for assessing the uniaxial compressive strength of rock. *Int. J. Rock Mech. Min. Sci.* **2001**, *38*, 981–994. [[CrossRef](#)]
44. Uyanık, O.; Sabbağ, N.; Uyanık, N.A.; Öncü, Z. Prediction of mechanical and physical properties of some sedimentary rocks from ultrasonic velocities. *Bull. Eng. Geol. Environ.* **2019**, *78*, 6003–6016. [[CrossRef](#)]
45. Kılıç, A.; Teymen, A. Determination of mechanical properties of rocks using simple methods. *Bull. Eng. Geol. Environ.* **2008**, *67*, 237–244. [[CrossRef](#)]
46. ASTM D2938-95; Standard Test Method for Unconfined Compressive Strength of Intact Rock Core Specimens. ASTM International: West Conshohocken, PA, USA, 2002.
47. ISRM. *Rock Characterization Testing and Monitoring*; Brown, E.T., Ed.; ISRM Suggested Methods; Pergamon Press: Oxford, UK, 1981; Volume 211.

48. ASTM D5731; Standard Test Method for Determination of the Point Load Strength Index of Rock. ASTM International: West Conshohocken, PA, USA, 2002.
49. ASTM D2845; Test Methods for Ultra Violet Velocities Determination. ASTM International: West Conshohocken, PA, USA, 1983.
50. Folk, R.L. *Petrology of Sedimentary Rocks*; Hemphill: Austin, TX, USA, 1974; 600p.
51. Dunham, R.J. *Classification of Carbonate Rocks According to Depositional Textures*; American Association of Petroleum Geologists: Tulsa, OK, USA, 1962; pp. 108–121.
52. Zhou, J.; Huang, S.; Qiu, Y. Optimization of random forest through the use of MVO, GWO and MFO in evaluating the stability of underground entry-type excavations. *Tunn. Undergr. Space Technol.* **2022**, *124*, 104494. [\[CrossRef\]](#)
53. Mohri, M.; Rostamizadeh, A.; Talwalkar, A. Foundations of Machine Learning. In *Adaptive Computation and Machine Learning Series*; MIT Press: Cambridge, MA, USA, 2018.
54. Liaw, A.; Wiener, M. Classification and Regression by Random Forest. *R News* **2002**, *2*, 18–22.
55. Harris, J.; Grunsky, E.C. Predictive lithological mapping of Canada's North using Random Forest classification applied to geophysical and geochemical data. *Comput. Geosci.* **2015**, *80*, 9–25. [\[CrossRef\]](#)
56. James, G.; Witten, D.; Hastie, T.; Tibshirani, R. *An Introduction to Statistical Learning*; Springer: Berlin/Heidelberg, Germany, 2013; Volume 112, 607p.
57. Zhu, B.; Zhong, Q.; Chen, Y.; Liao, S.; Li, Z.; Shi, K.; Sotelo, M.A. A Novel Reconstruction Method for Temperature Distribution Measurement Based on Ultrasonic Tomography. *IEEE Trans. Ultrason. Ferroelectr. Freq. Control* **2022**, *69*, 2352–2370. [\[CrossRef\]](#)
58. Raja, M.N.A.; Jaffar, S.T.A.; Bardhan, A.; Shukla, S.K. Predicting and validating the load-settlement behavior of large-scale geosynthetic-reinforced soil abutments using hybrid intelligent modeling. *JRMGE* **2023**, *15*, 773–788.
59. Vapnik, V.N. *Statistical Learning Theory*; Wiley: New York, NY, USA, 1998; p. 736.
60. Fallah, M.; Pirali Zefrehei, A.R.; Hedayati, S.A.; Bagheri, T. Comparison of temporal and spatial patterns of water quality parameters in Anzali Wetland (southwest of the Caspian Sea) using Support vector machine model. *Casp. J. Environ. Sci.* **2021**, *19*, 95–104.
61. Kookalani, S.; Cheng, B. Structural Analysis of GFRP Elastic Gridshell Structures by Particle Swarm Optimization and Least Square Support Vector Machine Algorithms. *J. Civ. Eng. Mater. Appl.* **2021**, *5*, 12–23.
62. Yang, H.; Wang, Z.; Song, K. A new hybrid grey wolf optimizer-feature weighted-multiple kernel-support vector regression technique to predict TBM performance. *Eng. Comput.* **2020**, *38*, 2469–2485. [\[CrossRef\]](#)
63. Yang, H.; Song, K.; Zhou, J. Automated Recognition Model of Geomechanical Information Based on Operational Data of Tunneling Boring Machines. *Rock Mech. Rock Eng.* **2022**, *55*, 1499–1516. [\[CrossRef\]](#)
64. Duda, R.O.; Hart, P.E.; Stork, D.G. *Pattern Classification*; John Wiley & Sons: Hoboken, NJ, USA, 2012; Volume 3, pp. 731–739.
65. Tharwat, A.; Ghanem, A.M.; Hassanien, A.E. Three different classifiers for facial age estimation based on k-nearest neighbor. In *Proceedings of the 2013 9th International Computer Engineering Conference (ICENCO)*, Giza, Egypt, 28–29 December 2013; IEEE: Piscataway, NJ, USA, 2013; pp. 55–60.
66. Aghighi, F.; Aghighi, H.; Ebadati, O.M. Evaluation of the efficiency of SVM and KNN Classification algorithms to extract urban effects from LiDAR cloud points. In *Second International Conference on Knowledge-Based Research in Computer Engineering & Information Technology*, Tehran, Iran, 30 September 2016; Majlisi University: Mobarakeh, Iran, 2017. (In Persian)
67. Saed, S.A.; Kamboozia, N.; Ziari, H.; Hofko, B. Experimental assessment and modeling of fracture and fatigue resistance of aged stone matrix asphalt (SMA) mixtures containing RAP materials and warm-mix additive using ANFIS method. *Mater. Struct.* **2021**, *54*, 225. [\[CrossRef\]](#)
68. Sobhani, B.; Safarianzengir, V. Monitoring and prediction of drought using TIBI fuzzy index in Iran. *Casp. J. Environ. Sci.* **2020**, *18*, 237–250.
69. Jang, J.S.R. ANFIS: Adaptive network based fuzzy inference system. *IEEE Trans. Syst. Man Cybern.* **1993**, *23*, 665–685. [\[CrossRef\]](#)
70. Moshahedi, A.; Mehranfar, N.A. Comprehensive Design for a Manufacturing System using Predictive Fuzzy Models. *J. Res. Sci. Eng. Technol.* **2021**, *9*, 1–23. [\[CrossRef\]](#)
71. Mokhberi, M.; Khademi, H. The use of stone columns to reduce the settlement of swelling soil using numerical modeling. *J. Civ. Eng. Mater. Appl.* **2017**, *1*, 45–60. [\[CrossRef\]](#)
72. Rastegarnia, A.; Lashkaripour, G.R.; Sharifi Teshnizi, E.; Ghafoori, M. Evaluation of engineering characteristics and estimation of dynamic properties of clay-bearing rocks. *Environ. Earth Sci.* **2021**, *80*, 621. [\[CrossRef\]](#)
73. Mikaeil, R.; Esmaeilzade, A.; Shaffiee Haghsheenas, S. Investigation of the Relationship Between Schimazek's F-Abrasiveness Factor and Current Consumption in Rock Cutting Process. *J. Civ. Eng. Mater. Appl.* **2021**, *5*, 47–55.
74. Keykhah, H.; Dahan Zadeh, B. Stability Analysis of Upstream Slope of Earthen Dams Using the Finite Element method Against Sudden Change in the Water Surface of the Reservoir, Case Study: Ilam Earthen Dam in Ilam Province. *J. Civ. Eng. Mater. Appl.* **2018**, *2*, 24–30.
75. Taheri, S.; Ziad, H. Analysis and Comparison of Moisture Sensitivity and Mechanical Strength of Asphalt Mixtures Containing Additives and Carbon Reinforcement. *J. Civ. Eng. Mater. Appl.* **2021**, *5*, 1–8.
76. Sobhani, J.; Jafarpour, F.; Firozyar, F.; Pourkhorshidi, A.R. Simulated C3A Effects on the Chloride Binding in Portland Cement with NaCl and CaCl₂ Cations. *J. Civ. Eng. Mater. Appl.* **2022**, *6*, 41–54.

77. Liu, B.; Yang, H.; Karekal, S. Effect of water content on argillization of mudstone during the tunneling process. *Rock Mech. Rock Eng.* **2020**, *53*, 799–813. [\[CrossRef\]](#)
78. Guo, Y.; Luo, L.; Wang, C. Research on Fault Activation and Its Influencing Factors on the Barrier Effect of Rock Mass Movement Induced by Mining. *Appl. Sci.* **2023**, *13*, 651. [\[CrossRef\]](#)
79. Yang, H.Q.; Li, Z.; Jie, T.Q.; Zhang, Z.Q. Effects of joints on the cutting behavior of disc cutter running on the jointed rock mass. *Tunn. Undergr. Space Technol.* **2018**, *81*, 112–120. [\[CrossRef\]](#)
80. Peng, J.; Xu, C.; Dai, B.; Sun, L.; Feng, J.; Huang, Q. Numerical Investigation of Brittleness Effect on Strength and Microcracking Behavior of Crystalline Rock. *Int. J. Geomech.* **2022**, *22*, 4022178. [\[CrossRef\]](#)
81. Ghavami, S.; Rajabi, M. Investigating the Influence of the Combination of Cement Kiln Dust and Fly Ash on Compaction and Strength Characteristics of High-Plasticity Clays. *J. Civ. Eng. Mater. Appl.* **2021**, *5*, 9–16.
82. Xiao, D.; Hu, Y.; Wang, Y.; Deng, H.; Zhang, J.; Tang, B.; Li, G. Wellbore cooling and heat energy utilization method for deep shale gas horizontal well drilling. *Appl. Therm. Eng.* **2022**, *213*, 118684. [\[CrossRef\]](#)
83. Rastegarnia, A.; Lashkaripour, G.R.; Ghafoori, M.; Farrokhad, S.S. Assessment of the engineering geological characteristics of the Bazoft dam site, SW Iran. *Q. J. Eng. Geol. Hydrogeol.* **2019**, *52*, 360–374. [\[CrossRef\]](#)
84. Kurtulus, C.; Bozkurt, A.; Endes, H. Physical and mechanical properties of serpentinized ultrabasic rocks in NW Turkey. *Pure Appl. Geophys.* **2012**, *169*, 1205–1215. [\[CrossRef\]](#)
85. Yagiz, S.; Sezer, E.A.; Gokceoglu, C. Artificial neural networks and nonlinear regression techniques to assess the influence of slake durability cycles on the prediction of uniaxial compressive strength and modulus of elasticity for carbonate rocks. *Int. J. Numer. Anal. Methods Géoméch.* **2012**, *36*, 1636–1650. [\[CrossRef\]](#)
86. Shirnezhad, Z.; Azma, A.; Foong, L.K.; Jahangir, A.; Rastegarnia, A. Assessment of water resources quality of a karstic aquifer in the Southwest of Iran. *Bull. Eng. Geol. Environ.* **2021**, *80*, 71–92. [\[CrossRef\]](#)
87. Shayesteh, A.; Ghasemisalehabadi, E.; Khordehbinan, M.W.; Rostami, T. Finite element method in statistical analysis of flexible pavement. *J. Mar. Sci. Technol.* **2017**, *25*, 15.
88. Rustamovich Sultanbekov, I.; Yurievna Myshkina, I.; Yurievna Gruditsyna, L. Development of an application for creation and learning of neural networks to utilize in environmental sciences. *Casp. J. Environ. Sci.* **2020**, *18*, 595–601.
89. Tabatabaei, M.; Salehpour Jam, A. Optimization of sediment rating curve coefficients using evolutionary algorithms and unsupervised artificial neural network. *Casp. J. Environ. Sci.* **2017**, *15*, 385–399.
90. Hecht-Nielsen, R. Kolmogorov's mapping neural network existence theorem. In Proceedings of the International Conference on Neural Networks, San Diego, CA, USA, 21–24 June 1987; IEEE Press: New York, NY, USA, 1987; Volume 3, pp. 11–14.
91. Hush, D. Classification with neural networks: A performance analysis. In Proceedings of the IEEE International Conference on Systems Engineering, Fairborn, OH, USA, 24–26 August 1989; IEEE: Piscataway, NJ, USA, 1989; pp. 277–280.
92. Ripley, B.D. *Statistical Aspects of Neural Networks*; Barndorff-Nielsen, O.E., Jensen, J.L., Kendall, W.S., Eds.; Networks and Chaos—Statistical and Probabilistic Aspects; Chapman and Hall: London, UK, 1993; pp. 40–123.
93. Paola, J.D. *Neural Network Classification of Multispectral Imagery*; The University of Arizona: Tucson, AZ, USA, 1994.
94. Wang, C. A Theory of Generalization in Learning Machines with Neural Application. Ph.D. Thesis, The University of Pennsylvania, Philadelphia, PA, USA, 1994.
95. Kaastra, I.; Boyd, M. Designing a neural network for forecasting financial and economic time series. *Neurocomputing* **1996**, *10*, 215–236. [\[CrossRef\]](#)
96. Kanellopoulos, I.; Wilkinson, G.G. Strategies and best practice for neural network image classification. *Int. J. Remote Sens.* **1997**, *18*, 711–725. [\[CrossRef\]](#)
97. Kavyanifar, B.; Tavakoli, B.; Torkaman, J.; Mohammad Taheri, A.; Ahmadi Orkomi, A. Coastal solid waste prediction by applying machine learning approaches (Case study: Noor, Mazandaran Province, Iran). *Casp. J. Environ. Sci.* **2020**, *18*, 227–236.
98. Rashidi Tazhan, O.; Pir Bavaghar, M.; Ghazanfari, H. Detecting pollarded stands in Northern Zagros forests, using artificial neural network classifier on multi-temporal landsat-8 (OLI) imageries (case study: Armarde, Baneh). *Casp. J. Environ. Sci.* **2019**, *17*, 83–96.
99. Dianati Tilaki, G.A.; Ahmadi Jolandan, M.; Gholami, V. Rangelands production modeling using an artificial neural network (ANN) and geographic information system (GIS) in Baladeh rangelands, North Iran. *Casp. J. Environ. Sci.* **2020**, *18*, 277–290.
100. Zhan, C.; Dai, Z.; Soltanian, M.R.; De Barros, F.P. Data-Worth Analysis for Heterogeneous Subsurface Structure Identification With a Stochastic Deep Learning Framework. *Water Resour. Res.* **2022**, *58*, e2022WR033241. [\[CrossRef\]](#)
101. Vapnik, V.; Chervonenkis, A. The necessary and sufficient conditions for consistency in the empirical risk minimization method. *Pattern Recognit. Image Anal.* **1991**, *1*, 283–305.
102. Nguyen, H. Support vector regression approach with different kernel functions for predicting blast-induced ground vibration: A case study in an open-pit coal mine of Vietnam. *SN Appl. Sci.* **2019**, *1*, 283. [\[CrossRef\]](#)
103. Al-Anazi, A.F.; Gates, I.D. Support vector regression to predict porosity and permeability: Effect of sample size. *Comput. Geosci.* **2012**, *39*, 64–76. [\[CrossRef\]](#)

104. Khajehzadeh, M.; Taha, M.R.; Eslami, M. Opposition-based firefly algorithm for earth slope stability evaluation. *China Ocean Eng.* **2014**, *28*, 713–724. [[CrossRef](#)]
105. Zhou, J.; Shen, X.; Qiu, Y.; Shi, X.; Khandelwal, M. Cross-correlation stacking-based microseismic source location using three metaheuristic optimization algorithms. *Tunn. Undergr. Space Technol.* **2022**, *126*, 104570. [[CrossRef](#)]

Disclaimer/Publisher’s Note: The statements, opinions and data contained in all publications are solely those of the individual author(s) and contributor(s) and not of MDPI and/or the editor(s). MDPI and/or the editor(s) disclaim responsibility for any injury to people or property resulting from any ideas, methods, instructions or products referred to in the content.